Journal of
Materials Chemistry C

ROYAL SOCIETY
OF CHEMISTRY

PAPER

View Article Online
View Journal

Cite this: DOI: 10.1039/d5tc01476j

Tuning valley-Ohmic contacts and interfacial electronic properties in valley-polarized semiconductor/Dirac semimetal heterostructures†

Hao Guo,[ab] Yongqian Zhu,[ac] Jinbo Pan *[ac] and Shixuan Du[acd]

Understanding and modulating the contacts and valley states in valley-polarized electronic devices is essential for designing next-generation valleytronic computing and memory devices. In this work, a class of van der Waals heterostructures (vdWHs) based on the valley-polarized semiconductor GdI_2 and Dirac semimetals X (graphene, germanene, and SiGe) is designed, achieving intrinsic p-type Ohmic contacts with precise modulation of the interfacial electronic properties. Using density functional theory calculations, we reveal that X/GdI_2 vdWHs induce a significant band gap in the Dirac semimetals due to interlayer orbital hybridization. Additionally, the graphene/GdI_2 vdWH exhibits an intrinsic p-type half-valley Ohmic contact, while germanene/GdI_2 and SiGe/GdI_2 vdWHs form intrinsic p-type overall Ohmic contacts. Due to work function differences, the contact interfaces between GdI_2 and X result in a built-in electric field, as evidenced by the calculated charge density differences and electrostatic potentials. Furthermore, by adjusting the interlayer distance and applying electrostatic doping, the Schottky barrier heights and valley splitting in X/GdI_2 vdWHs can be precisely tuned, which facilitates transitions from a half-valley Ohmic contact to an overall Ohmic or Schottky contact, achieving valley-switching ON/OFF states at K and K′ points. This study provides strategies for realizing multi-state valley-polarized electronic devices through interface engineering of valley-polarized semiconductors and Dirac semimetals.

Received 9th April 2025,
Accepted 10th July 2025

DOI: 10.1039/d5tc01476j

rsc.li/materials-c

1. Introduction

Quantum materials with engineered magnetic orders and topological states have opened exciting opportunities for next-generation spintronic devices.[1–4] In particular, two-dimensional (2D) valley-polarized materials stand out due to their distinctive physical and electronic characteristics, offering significant potential for spintronic and valleytronic applications.[5–7] Unlike conventional 2D semiconductors, where the electronic properties are governed mainly by carrier density, valley-polarized semiconductors provide additional control through valley polarization states (K and K′), providing extra electronic degrees of freedom.[8,9] The coupling between valleys and spin degrees of freedom in 2D materials has led to significant advancements in valleytronics and spintronics, especially for devices that utilize spontaneous valley polarization.[7] This spin–valley coupling results in spin–valley locking, enabling selective control of spin and valley states for encoding and reading information.[10] Such a relationship provides unique opportunities for designing spintronic and valleytronic devices, offering advantages in multi-state storage and low-power information processing.[5] In recent years, numerous 2D materials with valley polarization have been reported, such as MX (M = Zr, Ru, Os; X = F, Cl, Br, I),[11–14] MI_2 (M = Sc, Y),[15] CeX_2 (X = F, Cl, Br),[16] GdX_2 (X = Cl, Br, I),[17–19] and transition-metal dichalcogenides (TMDs) under circularly polarized light.[20] Among them, the GdI_2 monolayer stands out for its remarkable valley splitting (149 meV) and high Curie temperature (241 K),[21] resulting from the joint effects of d-orbital magnetic exchange interactions and the f-orbital strong spin orbital coupling effect of the Gd atom. With its pronounced valley polarization and elevated Curie temperature, the GdI_2 monolayer holds great potential for forming an intrinsic half-valley Ohmic contact with semimetals at room temperature. Notably, the layered vdW bulk GdI_2 has already been successfully synthesized experimentally.[22] Due to its lower cleavage energy (0.26 J m^{-2})[21] than that of graphene (0.36 J m^{-2}),[23] the GdI_2 monolayer is highly likely to be exfoliated and easily transferred, demonstrating strong experimental feasibility for constructing valley-polarized logic devices.

---

[a] Beijing National Laboratory for Condensed Matter Physics, Institute of Physics, Chinese Academy of Sciences, Beijing 100190, China. E-mail: jbpan@iphy.ac.cn

[b] School of Urban Construction, Hebei Normal University of Science & Technology, Qinhuangdao 066004, China

[c] School of Physics, University of Chinese Academy of Sciences, Beijing 100049, China

[d] Songshan Lake Materials Laboratory, Dongguan 523808, Guangdong, China

† Electronic supplementary information (ESI) available. See DOI: https://doi.org/10.1039/d5tc01476j

Additionally, the electronic states of different valleys in 2D valley-polarized semiconductors exhibit distinct symmetry differences in the band structure, which can be tuned by external factors such as electric field,[24,25] magnetic field,[13,26] and strain engineering.[18,27–29] In valleytronics, accurately controlling valley polarization modulates electronic transport, enabling precise adjustment of device switching characteristics and performance, which is crucial for the development of next-generation valleytronic computing and memory technologies. For instance, monolayer SnS, due to its intrinsic electric field and tunable Berry curvature, can exhibit significantly enhanced valley-spin splitting and Berry curvature under biaxial compressive strain, thereby enhancing the stability of valley polarization and expanding the valleytronic material system with elastic tunability.[30] Another study revealed that constructing ScI_2/MSe_2 (M = Zr, Hf, Sn) heterostructures can induce a transition from in-plane to out-of-plane magnetization, significantly enhancing valley splitting up to 121 meV and greatly improving valley polarization performance.[31] Moreover, in a WSe_2/Fe_3GeTe_2 van der Waals heterostructure (vdWH), efficient injection of spin-polarized holes under bias induces significant valley polarization between the ±K valleys, demonstrating promising potential for application in scalable, room-temperature valleytronic devices and magneto-optoelectronic integration.[32]

However, integrating 2D materials into practical devices, particularly in the design and optimization of contact interfaces, remains challenging.[33–37] For example, in vdWHs formed between 2D semiconductors and monolayer metals, high-throughput calculations reveal that the Schottky barrier height (SBH) and contact type are primarily governed by the interfacial potential difference, charge transfer, and interfacial dipole moments.[38] Very recently, Ang *et al.* proposed the concept of half-valley Ohmic contact in the $RuCl_2$/graphene vdWH by hole doping, enabling precise carrier control by allowing current injection through the 'Ohmic valley' at low-dissipation, while suppressing it at the 'Schottky valley'.[39] This approach introduces a new tunable degree of freedom for regulation: valley-switching states, which are crucial for advancing valleytronic devices. Therefore, understanding and modulating the physical properties of the contact interfaces between valley-polarized semiconductors and metal electrodes are crucial for the practical applications of 2D valley-polarized semiconductors in multi-state computing, storage, and spintronics.

Here, we present a class of X/GdI_2 vdWHs, consisting of 2D Dirac semimetals X (X = graphene, germanene, and SiGe) and a GdI_2 monolayer with significant valley splitting. By exploring different atomic alignments, we constructed three distinct stacking modes for each X/GdI_2 vdWH, with the T1-type stacking mode showing the lowest binding energy and being identified as the most stable configuration. Upon interaction with GdI_2, the Dirac points of the Dirac semimetal X open large band gaps. When spin–orbit coupling (SOC) is considered, the projected band structures show that the graphene/GdI_2 vdWH exhibits intrinsic p-type half-valley Ohmic contacts, while both germanene/GdI_2 and SiGe/GdI_2 vdWHs form intrinsic p-type overall Ohmic contacts. The charge redistribution and built-in electric field at the interface induced by the work function difference between GdI_2 and Dirac semimetals are confirmed by the charge density difference and electrostatic potential. Furthermore, by modifying the interlayer distance and implementing electrostatic doping, the SBHs of X/GdI_2 vdWHs can be precisely tuned, enabling transitions between half-valley Ohmic contacts, overall Ohmic contacts, and overall Schottky contacts. Finally, we discuss the regulation of charge injection and valley-switching ON/OFF behavior in potential spintronic devices based on X/GdI_2 vdWHs under external fields. This study provides a novel perspective on valley-polarized semiconductors and offers theoretical guidance for designing low-power spintronic devices.

2. Methods and computational details

First-principles calculations were performed using density functional theory (DFT) as implemented in the Vienna *ab initio* Simulation Package (VASP).[40,41] The projector augmented wave (PAW) pseudopotentials[42] with valence electron configurations of $4f^7 5d^1 6s^2$ for Gd, $5s^2 5p^5$ for I, $2s^2 2p^2$ for C, $3s^2 3p^2$ for Si, and $4s^2 4p^2$ for Ge were employed to describe ion–electron interactions. The exchange–correlation functional was described using the generalized gradient approximation (GGA) with the Perdew, Burke and Ernzerhof (PBE) functional.[43] The HSE06 hybrid functional was used to calculate the band structure of monolayer GdI_2 in order to check the reliability of the electronic structure obtained from the PBE+U method. A vacuum space of 30 Å was added along the z-direction to eliminate the interaction between adjacent layers. The cutoff energy for the plane wave basis was set to 500 eV. The first Brillouin zone was sampled using a converged Γ-centered k-point mesh of size $15 \times 15 \times 1$ for structural relaxation and electronic analyses. The geometrical structures were fully relaxed until the forces and energies converged to 0.01 eV Å^{-1} and 1.0×10^{-5} eV, respectively. Due to the strong correlation effects of Gd-4f electrons in the GdI_2 layer, the GGA+U method[44] was used to describe its magnetic anisotropy of the GdI_2 layer. The Hubbard U parameter was set to 4.6 eV.[18] van der Waals density functional correction within the Grimme scheme (DFT-D3) was implemented to account for the van der Waals interaction.[45,46] SOC was considered for the calculation of projected band structures.

3. Results and discussion

3.1. Structural parameters and stabilities

The GdI_2 monolayer has a 2H-MoS_2 type hexagonal crystal structure with a $p\bar{6}m2$ space group and an I–Gd–I sandwich stacking along the z-direction.[17,47] The relaxed lattice constants of the pristine GdI_2 monolayer are $a = b = 4.14$ Å, as shown in Fig. 1a, which are in good agreement with previous theoretical results (4.139 Å).[17] The optimized lattice constants of graphene, germanene, and SiGe monolayers are 2.46 Å, 4.04 Å, and 3.94 Å, respectively, as listed in Table 1, which are consistent with previously reported experimental and theoretical values.[48–51] With fixed lattice constants of the GdI_2 monolayer, we

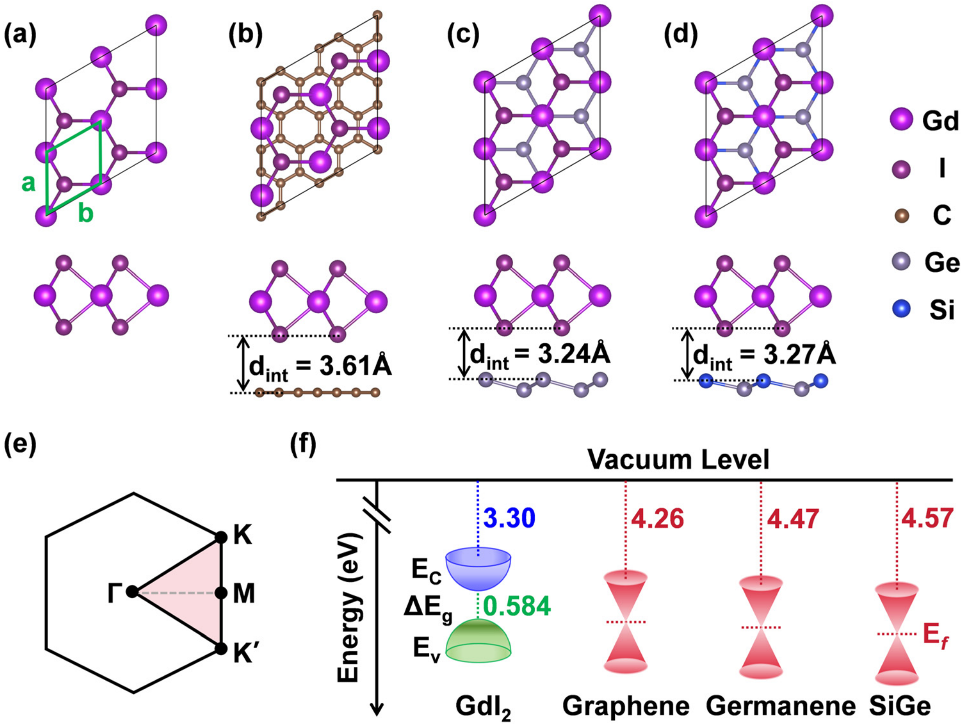

Fig. 1 Structures, Brillouin zone and band alignments. The top and side views of (a) a pristine GdI_2 monolayer, (b) T1-type graphene/GdI_2, (c) T1-type germanene/GdI_2, and (d) T1-type SiGe/GdI_2 vdWHs. The green rhombus denotes the unit cell of the GdI_2 monolayer. (e) The first Brillouin zone with high-symmetry points. (f) The band alignments of GdI_2 and Dirac semimetals X, graphene, germanene and SiGe. ΔE_g, E_C, and E_V denote the band gap, the conduction band edge, and the valence band edge of the GdI_2 monolayer, respectively. E_f represents the Fermi level of Dirac semimetals X.

constructed the X/GdI_2 vdWHs (X = graphene, germanene, and SiGe) by stacking the 2 × 2 supercells of GdI_2 on the $2\sqrt{3} \times 2\sqrt{3}$ supercells of graphene, 2 × 2 supercells of germanene, and 2 × 2 supercells of SiGe with lattice mismatches of 2.90%, 2.47%, and 5.07%, respectively. The strain induced by lattice mismatch has no significant impact on the Dirac points or the overall electronic properties of the Dirac semimetals, as shown in Fig. S1 (ESI†). Moreover, owing to the different atomic alignments, we considered three different stacking modes for X/GdI_2 by shifting GdI_2 along the a and $a + b$ directions, labeled as T1, T2, and T3, as shown in Fig. S2a–i (ESI†), respectively.

Moreover, in order to evaluate the structural stability, the binding energies (E_b) of X/GdI_2 vdWHs with different stacking modes are calculated according to the following formula:

$$E_b = \frac{E_{X/GdI_2} - E_X - E_{GdI_2}}{N} \quad (1)$$

where $N = 4$ is the number of GdI_2 unit cells in X/GdI_2 vdWHs; E_{X/GdI_2}, E_X, and E_{GdI_2} are the total energies of X/GdI_2 vdWHs, isolated Dirac semimetals X (X = graphene, germanene, and SiGe) and isolated GdI_2 monolayer, respectively. Based on the calculated results presented in Table S1 (ESI†), all binding energies of X/GdI_2 vdWHs in different stacking modes are negative, indicating that their formation is thermodynamically exothermic and easy to be synthesized experimentally. Specifically, the binding energies of T1-type graphene/GdI_2, germanene/GdI_2, and SiGe/GdI_2 vdWH are −0.954 eV per atom, −0.937 eV per atom, and −0.932 eV per atom, respectively, which are lower than those of T2- and T3-type stacking modes. These results demonstrate that the T1-type stacking configurations of X/GdI_2 vdWHs are more energy favorable. Therefore, we focus on and discuss the structure, electronic, and magnetic properties of T1-type X/GdI_2 vdWHs in the following sections.

Table 1 Lattice constants (a and b) of Dirac semimetals, lattice mismatches (δ) between GdI_2 and Dirac semimetals, equilibrium interlayer distances (d_{int}) and binding energies (E_b) of vdWHs, work functions of the Dirac semimetals (W_m), work functions of the vdWHs (W_{hs}) and their differences ($\Delta W = W_m - W_{hs}$), p-type SBHs without SOC at the K and K′ points ($\Phi_{p\text{-}K/K'}$), p-type SBHs at the K point ($\Phi_{p\text{-}K}$) and the K′ point ($\Phi_{p\text{-}K'}$) of the vdWHs with a positive magnetic moment along the +z-direction in the presence of SOC

vdWHs	$a = b$ (Å)	δ (%)	E_b (eV)	d_{int} (Å)	W_m (eV)	W_{hs} (eV)	ΔW (eV)	$\Phi_{p\text{-}K/K'}$ (meV)	$\Phi_{p\text{-}K}$ (meV)	$\Phi_{p\text{-}K'}$ (meV)
Graphene/GdI_2	2.46 2.46[48]	2.90	−0.954	3.61	4.26 4.24[52]	3.82	0.44	6	−19	130
Germanene/GdI_2	4.04 4.034[49]	2.47	−0.937	3.24	4.47 4.45[53]	4.35	0.12	−115	−179	−37
SiGe/GdI_2	3.94 3.939[49]	5.07	−0.932	3.27	4.57 4.46[54]	4.38	0.19	−131	−213	−64

The top and side views of optimized T1-type X/GdI_2 vdWHs are shown in Fig. 1b–d. The equilibrium interlayer distances (d_{int}) of relaxed T1-type graphene/GdI_2, germanene/GdI_2, and SiGe/GdI_2 are 3.61 Å, 3.24 Å, and 3.27 Å, respectively, which are much larger than the sum of the covalent radii of I and C (Ge, Si) atoms, indicating weak vdW interactions between the GdI_2 and Dirac semimetals X.

3.2. Magnetic and electronic properties

Due to the contribution of the half-filled f and d orbitals of the Gd atom, the calculated magnetic moment of the GdI_2 monolayer is 7.434μ_B/Gd, which is in good agreement with the previously reported value (7.446μ_B/Gd).[18] Fig. 1e shows the first Brillouin zone with high-symmetry points of the GdI_2 monolayer. As shown in Fig. S3a and b (ESI†), the GdI_2 monolayer is a semiconductor with indirect band gap values of 1.10 eV (HSE06 + SOC) and 0.584 eV (PBE+U), which are in good agreement with the previous studies.[18,21,27] Note that the HSE06 and PBE+U functionals produce quite similar band structures, with negligible differences in the band profile except for the size of the band gap. Therefore, to balance accuracy and computational efficiency, PBE+U is adopted for all calculations of monolayer GdI_2 and its vdWHs unless otherwise specified. In addition, the band structure reveals that the valley splitting of the GdI_2 monolayer is 147 meV, which is consistent with the previously reported value (149 meV)[18] and larger than those of GdF_2 (55 meV), $GdCl_2$ (38 meV), and $GdBr_2$ (82 meV).[19] By applying a reversed external magnetic field, the magnetization direction of the Gd atoms in the GdI_2 monolayer can be effectively switched, achieving a reversal from $+z$ to $-z$. As shown in Fig. S3c and d (ESI†), this magnetization reversal (M-reversing) further leads to the inversion of both spin and valley polarization in the GdI_2 monolayer, which is consistent with previous reports.[18,55]

The work function, defined as the energy difference between the vacuum level and the Fermi level ($W = E_{vac} - E_f$), represents the minimum energy required to remove an electron from the material surface to a point in the vacuum immediately outside the material.[56,57] The work function of the isolated GdI_2 monolayer is 3.67 eV, which is less than those of graphene (4.26 eV), germanene (4.47 eV), and SiGe (4.57 eV), as listed in Fig. 1f and Table 1. Due to the difference in work functions, the alignment process causes charge redistribution at the interface, thereby adjusting the work function of the vdWHs. Charge transfer at the metal–semiconductor contact interface plays a crucial role in determining the performance of electronic devices.[58] The calculations show that electrons are transferred from GdI_2 to Dirac semimetals X upon the formation of their vdWHs, as illustrated in Fig. 2a–c. This behavior is opposite to what is observed in $RuCl_2$/graphene and $NbSe_2$/graphene vdWHs since the work functions of $RuCl_2$ and $NbSe_2$ are higher than that of graphene.[39] Consequently, the Dirac semimetals X accumulate electrons, while GdI_2 experiences hole accumulation due to electron dissipation, creating a built-in electric field (E) from GdI_2 to the Dirac semimetals X, as shown in Fig. 2d.

Upon stacking into vdWHs, electron transfer and redistribution at the contact interface induce alignment of the Fermi levels of GdI_2 and the Dirac semimetals, promoting the establishment of thermal equilibrium throughout the system. Specifically, the work function of the vdWHs tends to align more closely with that of the material that undergoes less carrier transfer, *i.e.*, the material more strongly influenced by the Fermi level pinning (FLP). Here, FLP refers to an interfacial effect that arises when a metal is brought into contact with a

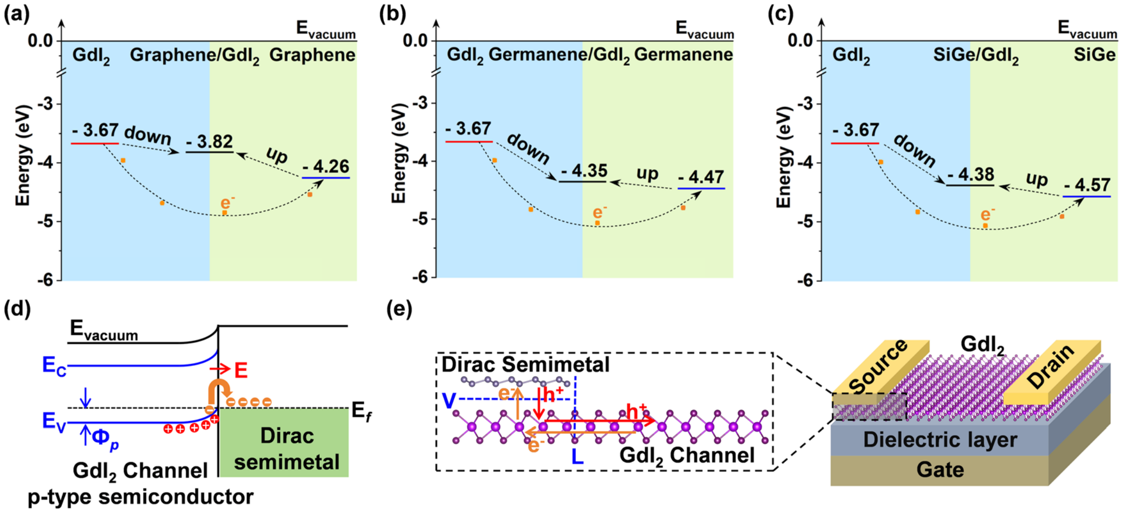

Fig. 2 Changes in the work functions and the direction of electron transfer after the formation of the X/GdI_2 vdWHs. The movement of the Fermi levels, the changes in the work functions, and the transfer direction of electrons in the process of forming (a) graphene/GdI_2, (b) germanene/GdI_2, and (c) SiGe/GdI_2 vdWHs. The orange dots represent the flowing electrons. (d) Schematic band diagram of the GdI_2 channel and Dirac semimetals X. E_C and E_V denote the conduction band edge and the valence band edge of GdI_2 in the X/GdI_2 vdWHs, respectively. Φ_p, E_f, and E represent the p-type SBHs, the Fermi level, and the built-in electric field at the interface in X/GdI_2 vdWHs, respectively. (e) Schematic of a Dirac semimetal-GdI_2 contacted FET and the carrier transfer path. The blue dashed lines labeled V and L represent the vertical interface between the Dirac semimetal and the underlying GdI_2 and the lateral interface between the channel GdI_2 and contacted GdI_2, respectively.

semiconductor. A large number of surface and interface states typically exist at the metal–semiconductor interface, which can pin the Fermi level of the heterostructure at a fixed position and prevent it from being effectively tuned.[34] The presence of FLP weakens the ability of the metal's work function to modulate the contact barrier, leading to increased contact resistance and a reduction in overall device performance.[59] In comparison, due to its higher carrier concentration and lower density of states, graphene is more susceptible to interfacial charge transfer and Fermi level adjustment. As a result, the work function of graphene/GdI_2 (3.82 eV) is closer to that of GdI_2 (3.67 eV). In contrast, due to the lower carrier concentrations, germanene and SiGe experience greater charge redistribution at the interface, forming a stronger interfacial dipole. Consequently, FLP is more pronounced on the Dirac semimetal side, leading to the overall work functions of germanene/GdI_2 (4.35 eV) and SiGe/GdI_2 (4.38 eV) being closer to those of germanene (4.47 eV) and SiGe (4.57 eV). Thus, the work function of graphene/GdI_2 is predominantly determined by GdI_2, while the work functions of germanene/GdI_2 and SiGe/GdI_2 are mainly governed by germanene and SiGe, respectively.

Moreover, Fig. 2d shows that electrons from the valence band of the GdI_2 monolayer transfer to the Dirac semimetals across the Schottky barrier, resulting in an increased hole concentration at the GdI_2 contact interface and the formation of holes' anti-barrier. At the same time, the energy band edges of the p-type semiconductor GdI_2 shift upward. If X/GdI_2 vdWHs form Ohmic contacts, electrons transferring from GdI_2 to the Dirac semimetals X becomes easier, free from the obstruction of the Schottky barrier. This phenomenon can be utilized to design FETs with low power consumption and high switching efficiency, as illustrated in Fig. 2e. It is worth noting that stronger interlayer interactions modify the band structure of GdI_2, causing the energy at the Γ point in the top valence band of the spin-up channel of GdI_2 is higher than that at the K and K′ points.

The SBH is a critical parameter for evaluating the interfacial charge transfer resistance of metal/semiconductor contacts. According to the Schottky–Mott rules, the n-type SBH (Φ_n) and p-type SBH (Φ_p) can be calculated using the equations:

$$\Phi_n = E_C - E_f, \quad \Phi_p = E_f - E_V \tag{2}$$

where E_C and E_V represent the CBM and VBM of GdI_2 in the projected band structures of the X/GdI_2 vdWHs, respectively. When 0 eV $< \Phi_n < \Phi_p$ or 0 eV $< \Phi_p < \Phi_n$, n-type or p-type Schottky contacts are formed, respectively. However, when $\Phi_n \leq 0$ eV or $\Phi_p \leq 0$ eV, n-type or p-type Ohmic contacts are established.[58]

When SOC is not considered, the schematic drawing of the band structure contributed by GdI_2 at the K and K′ points in X/GdI_2 vdWHs with no valley splitting is shown in Fig. 3a. The projected band structures of X/GdI_2, as shown in Fig. S4a–c (ESI†), reveal that the Dirac points of Dirac semimetals X in graphene/GdI_2, germanene/GdI_2 and SiGe/GdI_2 deviate downward from the Fermi level by about 188 meV, 179 meV

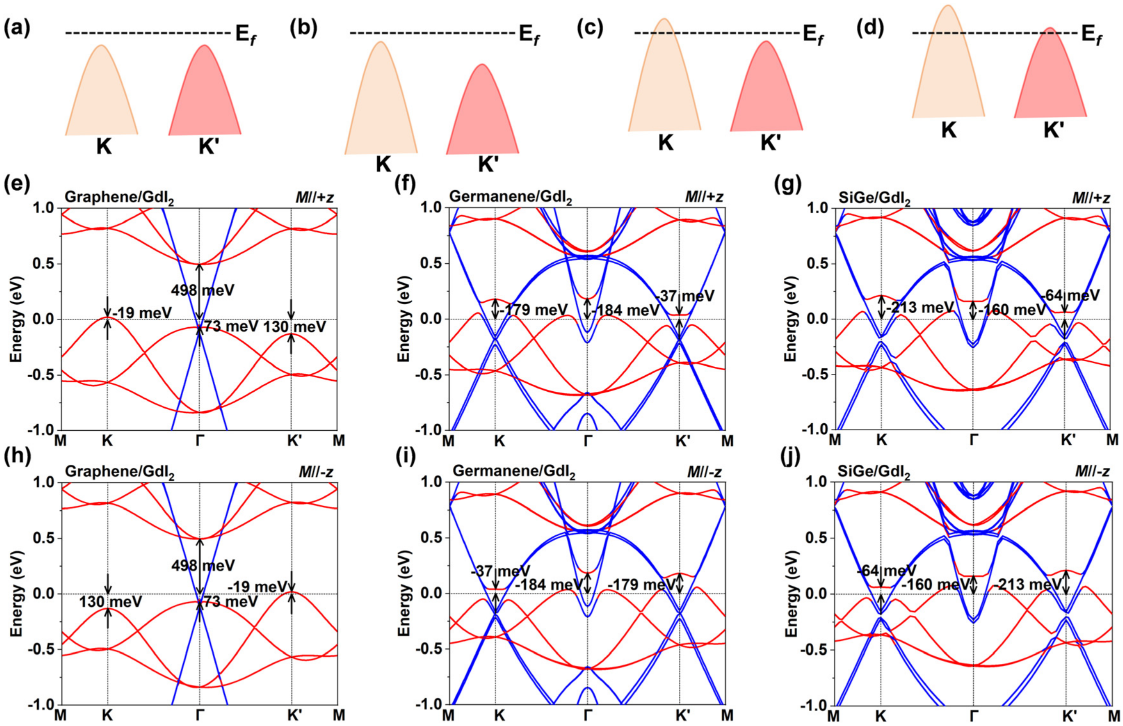

Fig. 3 Projected band structures of X/GdI_2 vdWHs. Schematic diagrams of the band structure at the K and K′ points with (a) no valley splitting, (b) p-type overall Schottky contact, (c) p-type half-valley Ohmic contact, and (d) p-type overall Ohmic contact. The brown and pink lines represent the valence band edges of GdI_2 at the K and K′ points, respectively. Projected band structures with the positive and negative magnetic moments along the z-direction of (e) and (h) graphene/GdI_2, (f) and (i) germanene/GdI_2, and (g) and (j) SiGe/GdI_2 in the presence of SOC, respectively. The red and blue lines in the band structures represent the contributions from GdI_2 and graphene, respectively. The Fermi level (E_f) is set to 0 eV.

and 185 meV, respectively. More interestingly, the exchange interaction between the electrons of the Dirac semimetals and the local magnetic moment induced by GdI_2, originating from the d and f orbitals of the Gd atom, leads to a modification of the electronic structure near the Dirac point, resulting in the opening of a band gap. This interaction causes spin-up and spin-down electrons to experience distinct effective potentials, thereby giving rise to an asymmetric band gap and manifesting a spin-dependent band gap. Specifically, the spin-up (spin-down) channel of GdI_2 induces band gaps of 7 meV (4 meV) in graphene, 30 meV (4 meV) in germanene, and 19 meV (10 meV) in SiGe, respectively. However, since the SOC effect can induce valley splitting in the GdI_2 monolayer, the X/GdI_2 vdWHs may exhibit a p-type overall Schottky contact, half-valley Ohmic contact, and overall Ohmic contact at the K and K′ points, as shown in Fig. 3b–d, respectively. Fig. 3e shows the p-type SBH at the K (K′) point of the graphene/GdI_2 vdWH is −19 meV (130 meV), while the n-type SBH at the Γ point is 498 meV. The result indicates that the graphene/GdI_2 vdWH forms a p-type half-valley Ohmic contact at the K point. However, the p-type SBHs at the K and K′ points of the germanene/GdI_2 vdWH are −179 meV and −37 meV, as shown in Fig. 3f, indicating that germanene/GdI_2 forms a p-type overall Ohmic contact. Similarly, the SiGe/GdI_2 vdWH also exhibits a p-type overall Ohmic contact, with SBHs of −213 meV and −64 meV at the K and K′ points, respectively, as shown in Fig. 3g. The p-type SBHs at the K and K′ points of germanene/GdI_2 and SiGe/GdI_2 vdWHs are less than 0 eV, this implies that the valley polarization of GdI_2 at the K and K′ points is turned off, rendering both points conductive.

The intrinsic p-type half-valley Ohmic contact (graphene/GdI_2) and p-type overall Ohmic contact (germanene/GdI_2 and SiGe/GdI_2) are expected to have broader application in valleytronics devices than the artificially regulated half-valley and overall Ohmic contacts. More intriguingly, in the presence of SOC, the energy bands of germanene and SiGe in the X/GdI_2 vdWHs exhibit significant band splitting (blue lines), whereas graphene does not. This difference arises from the stronger interfacial hybridization between the sp^2 orbitals of germanene or SiGe and the orbitals of GdI_2, which disrupts the equivalence of the two sublattices within the monolayers. The resulting symmetry breaking lifts the band degeneracy and causes band splitting. In contrast, the relatively weaker interfacial interaction in graphene preserves its sublattice equivalence, preventing band splitting. Moreover, by reversing the magnetization direction from +z to −z, as shown in Fig. 3h–j, the valley polarization between the K and K′ points of the X/GdI_2 vdWHs can be flipped, while the absolute values of the valley splitting remain unaffected by the direction of magnetization. The reversal of out-of-plane ferroelectric polarization in the SiGe monolayer does not significantly affect the overall electronic properties or contact barrier of the SiGe/GdI_2 heterostructure, which remains a p-type Ohmic contact, as shown in Fig. S5 (ESI†).

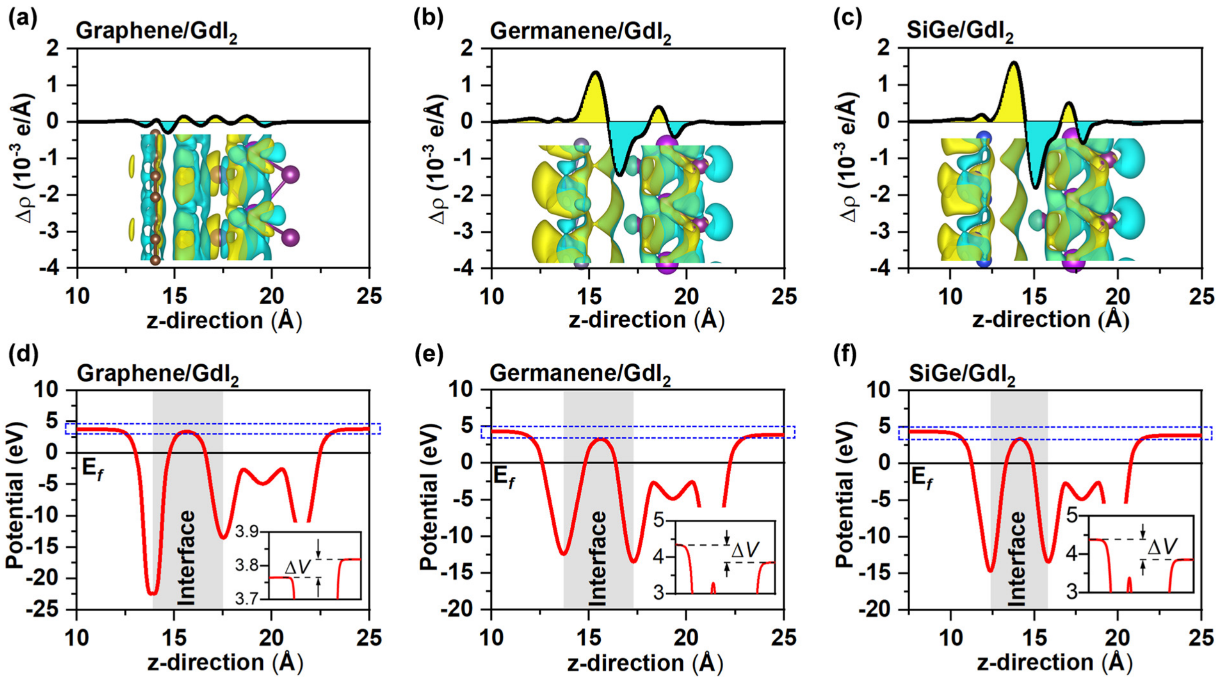

Fig. 4 Charge density difference and electrostatic potential. Plane-averaged charge density differences ($\Delta\rho$) along the z-direction of (a) graphene/GdI_2, (b) germanene/GdI_2, and (c) SiGe/GdI_2 vdWHs. The insets display the 3D charge density differences. The yellow and cyan regions represent charge accumulation and depletion, respectively. The isosurface values are set to 1×10^{-5} e Å^{-3}. Planar average electrostatic potential curves of (d) graphene/GdI_2, (e) germanene/GdI_2, and (f) SiGe/GdI_2 vdWHs along their z-directions. The gray shaded areas represent the contact interfaces of semimetal/GdI_2 vdWHs. The illustrations at the bottom right show partial enlargements (blue dashed lines). The Fermi level (E_f) is set to 0 eV. ΔV represents electrostatic potential difference.

As previously mentioned, the construction of X/GdI_2 vdWHs disrupts the original charge balances on the surface of the Dirac semimetals and GdI_2, causing the charge to redistribute until a new equilibrium is reached.[60] The charge redistribution at the interface between X and GdI_2 can be identified by analyzing the charge density differences ($\Delta\rho$), defined as:

$$\Delta\rho = \rho_{\mathrm{X/GdI_2}} - \rho_{\mathrm{X}} - \rho_{\mathrm{GdI_2}} \tag{3}$$

where $\rho_{\mathrm{X/GdI_2}}$, ρ_{X}, and $\rho_{\mathrm{GdI_2}}$ represent the charge densities of the X/GdI_2 vdWHs, the isolated Dirac semimetals X, and the isolated GdI_2 monolayer, respectively. The plane-averaged charge density differences and charge density differences of graphene/GdI_2, germanene/GdI_2, and SiGe/GdI_2 vdWHs are shown in Fig. 4a–c, respectively. It is evident that charge accumulation occurs on the Dirac semimetal side and depletion on the GdI_2 side, which is consistent with the direction of electron transfer previously analyzed based on the work function (Fig. 2a–c). Due to the larger interlayer distance (3.61 Å) between GdI_2 and graphene, charge transfer and dipole strength are weakened, resulting in weaker interlayer hybridization. In contrast, the smaller interlayer distances in germanene/GdI_2 (3.24 Å) and SiGe/GdI_2 (3.27 Å) lead to stronger interface hybridization, promoting charge redistribution. The different electron gain and loss of the Dirac semimetals X and the GdI_2 monolayer result in the formation of dipoles at their contact interfaces, inducing an electrostatic potential difference (ΔV), as shown in Fig. 4d–f. The electrostatic potential differences (ΔV) are 0.055 eV, 0.487 eV, and 0.523 eV in graphene/GdI_2, germanene/GdI_2, and SiGe/GdI_2 vdWHs, respectively. The combined analysis of charge density differences and electrostatic potential differences demonstrates that the charge accumulation and depletion at the germanene/GdI_2 and SiGe/GdI_2 interfaces are more pronounced than those at the graphene/GdI_2 interface, indicating a stronger interfacial dipole and enhanced charge transfer efficiency.

3.3. Tunable SBHs and valley states

Manipulating the SBHs for metal/semiconductor vdWHs is a key challenge in designing high-performance spintronic devices.[58] Recent studies have shown that adjusting the interlayer distance of vdWHs is an effective method to modulate the SBH and contact type in metal/semiconductor vdWHs, including graphene/SbX (X = P, As, Bi),[61] graphene/Au_2S,[62] Ti_3X_2/MoS_2 (X = B, C, N),[63] and graphene/MTe (M = Al, B).[64] This is primarily due to the fact that the interlayer distance in 2D vdWHs determines the strength and nature of the interlayer interactions, which directly affect the SBHs. By precisely tuning the interlayer spacing, it is possible to modulate the electronic properties of the contact, including the transition between Schottky and Ohmic contacts, thereby influencing the efficiency of charge and spin transport, which is critical for the performance of high-performance spintronic devices.

As shown in Fig. 5a, the interlayer distance can be modulated by applying vertical tensile or compressive strains along the *z*-direction, which can be experimentally achieved through vertical pressure or by inserting a hexagonal boron nitride (h-BN) buffer layer.[61,65] Fig. 5b–d show the p-type SBHs at the K and K′ points of X/GdI_2 vdWHs as a function of interlayer distances. Obviously, the p-type SBHs vary monotonically with interlayer distances, achieving a transition between negative and positive values. However, the p-type SBHs at the K point are consistently lower than those at the K′ point, and the difference between them exhibits only slight fluctuations with changes in the interlayer distance, indicating that the variation

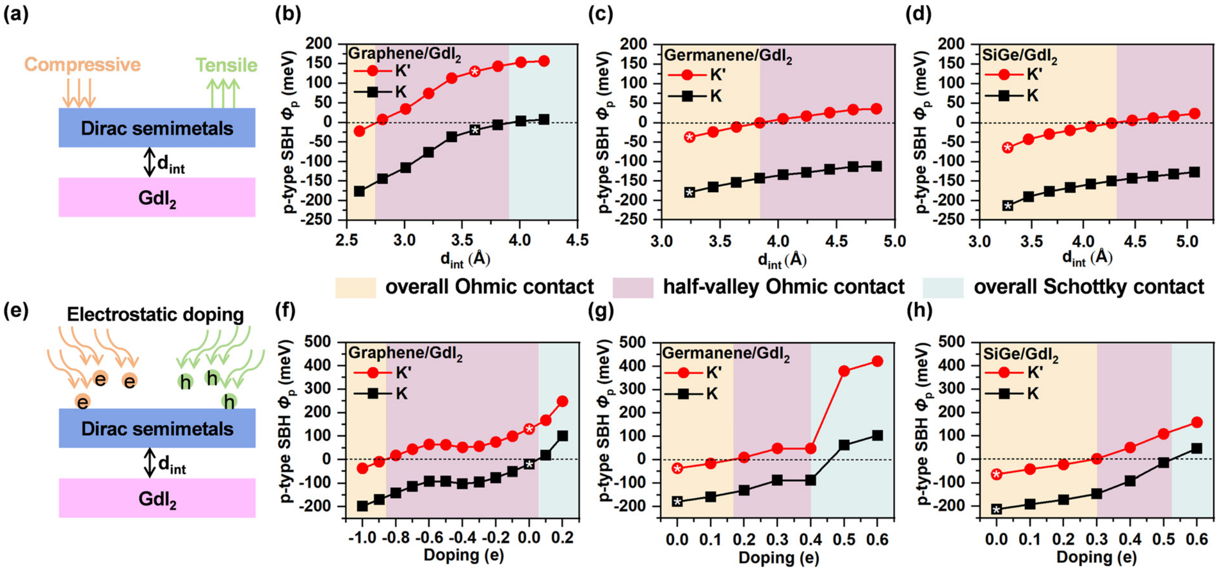

Fig. 5 Tunable p-type SBHs and contact type. (a) Schematic diagram of interlayer distance modulation through vertical compressive or tensile strains. The p-type SBHs at the K and K′ points as a function of interlayer distance for (b) graphene/GdI_2, (c) germanene/GdI_2, and (d) SiGe/GdI_2 vdWHs. (e) Schematic diagram of electron or hole doping. The p-type SBHs at the K and K′ points as a function of electron or hole doping for (f) graphene/GdI_2, (g) germanene/GdI_2, and (h) SiGe/GdI_2 vdWHs. The asterisks indicate the p-type SBHs of X/GdI_2 vdWHs at their initial equilibrium state. The positive and negative values of electrostatic doping represent electron doping and hole doping, respectively. The magnetic moment is aligned along the +*z*-direction, and the SOC effect is considered.

in interlayer distances has a minimal effect on the valley polarization of GdI_2. Specifically, as shown in Fig. 5b, when the interlayer distance of graphene/GdI_2 vdWH increases from 3.61 Å to more than 4.01 Å ($d_{int} \geq 4.01$ Å), the p-type SBHs at both the K and K′ points exceed 0 eV, indicating that the graphene/GdI_2 vdWH transforms from a p-type half-valley Ohmic contact to a p-type overall Schottky contact. However, for 2.61 Å $\leq d_{int} \leq$ 3.81 Å, the p-type SBH values at the K and K′ points remain positive and negative, respectively, implying that the graphene/GdI_2 vdWH retains an intrinsic p-type half-valley Ohmic contact. When $d_{int} \leq$ 2.61 Å, the p-type SBHs at both the K and K′ points of the graphene/GdI_2 vdWH drop below 0 eV, forming a p-type overall Ohmic contact. The projected band structure of the graphene/GdI_2 vdWH at different interlayer distances is shown in Fig. S6 (ESI†). Similarly, as shown in Fig. 5c and d, the germanene/GdI_2 (SiGe/GdI_2) vdWH can be transformed from the intrinsic p-type overall Ohmic contact to a p-type half-valley Ohmic contact by increasing the interlayer distance from 3.24 Å (3.27 Å) to 3.84 Å (4.47 Å). The projected band structures of the germanene/GdI_2 and SiGe/GdI_2 vdWHs at different interlayer distances are shown in Fig. S7 and S8 (ESI†), respectively. When the interlayer distance is increased to about 5 Å, germanene/GdI_2 and SiGe/GdI_2 vdWHs remain in the p-type half-valley Ohmic contact.

External electron or hole doping is also an effective method for modulating the electronic properties of 2D materials and their vdWHs by shifting the Fermi level.[66–68] As shown in Fig. 5e, the electrostatic doping can be achieved through the application of an external gate voltage.[69,70] From Fig. 5f, one can see that the electron doping exceeding 0.1 e transforms graphene/GdI_2 vdWH from the intrinsic p-type half-valley Ohmic contact to a p-type overall Schottky contact due to the reduced p-type SBH at the K point (−19 meV). When hole doping increases from 0 e to 0.8 e, although the p-type SBHs at the K and K′ points decrease with fluctuation, graphene/GdI_2 maintains the intrinsic p-type half-valley Ohmic contact.

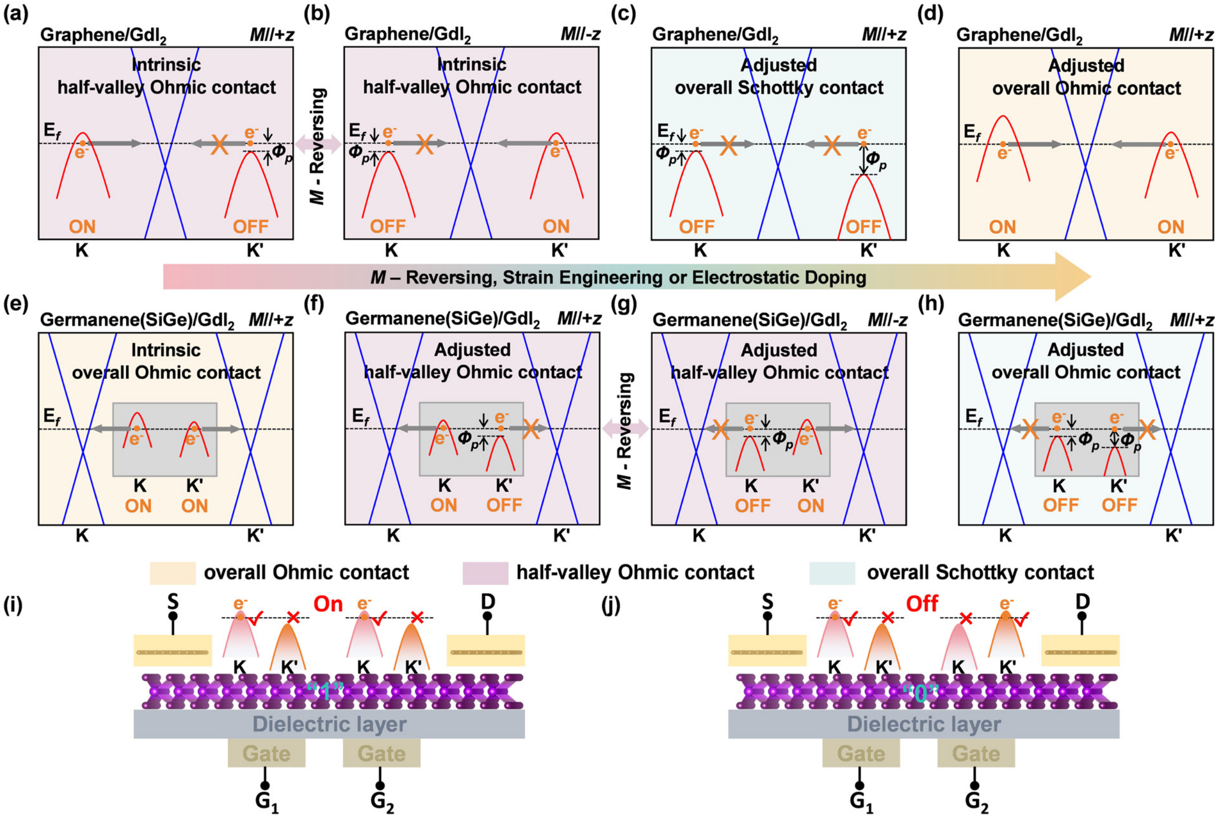

Fig. 6 Tunable contact types and valley-switching states of electronic transport. Intrinsic p-type half-valley Ohmic contact of graphene/GdI_2 vdWH with (a) +z and (b) −z magnetization directions. (c) Adjusted p-type overall Schottky contact and (d) p-type overall Ohmic contact of graphene/GdI_2 vdWH. (e) Intrinsic p-type overall Ohmic contact of germanene/GdI_2 and SiGe/GdI_2 vdWHs. Adjusted p-type half-valley Ohmic contact of germanene/GdI_2 and SiGe/GdI_2 vdWHs with (f) +z and (g) −z magnetization directions. (h) Adjusted p-type overall Schottky contact of germanene/GdI_2 and SiGe/GdI_2 vdWHs. The blue and red lines represent the energy bands with Dirac points of the Dirac semimetals X and the valence band edge of GdI_2 in X/GdI_2 vdWHs, respectively. The gray arrows indicate the electron transfer free paths of GdI_2 at the high-symmetry points K and K′ in the X/GdI_2 vdWHs (without Schottky barrier). The orange crosses indicate that the electron transfer is blocked (with Schottky barrier). E_f and Φ_p represent the Fermi level of the X/GdI_2 vdWHs and the p-type SBHs at the K or K′ point, respectively. The orange dots represent the freely flowing electrons. M-Reversing represents reversing the magnetization direction of Gd atoms from +z to −z. Schematic of the valley-state logic device featuring two gates, illustrating (i) the "On" state and (j) the "Off" state. S, D, and G denote the source, drain, and gate, respectively. The source and drain are in direct contact with the GdI_2 channel, while the two gates are separated from the GdI_2 channel by a dielectric layer. Dashed lines indicate the Fermi energy. The band alignment is determined by the directions of the gate electric fields.

However, graphene/GdI$_2$ vdWH can be transformed into a p-type overall Ohmic contact when the hole doping reaches 0.9 e. Since germanene/GdI$_2$ and SiGe/GdI$_2$ vdWHs exhibit intrinsic p-type overall Ohmic contacts, regulation of their SBHs and contact types can only be achieved by electron doping. Specifically, as shown in Fig. 5g and h, electron doping of 0.2 e (0.4 e) and 0.4 e (0.6 e) can induce germanene/GdI$_2$ (SiGe/GdI$_2$) to transition into a p-type half-valley Ohmic contact and p-type overall Schottky contact, respectively. The projected band structure of the graphene/GdI$_2$, germanene/GdI$_2$, SiGe/GdI$_2$ vdWHs with different electrostatic doping are shown in Fig. S9–S11 (ESI†), respectively.

Finally, we discuss the charge injection and valley switching at the K and K$'$ points under the action of *M*-reversing, strain engineering or electrostatic doping, as shown in Fig. 6. In the intrinsic p-type half-valley Ohmic contact of the graphene/GdI$_2$ vdWH, as shown in Fig. 6a, electrons originating from GdI$_2$ can be injected into graphene through the K valley (ON), while the K$'$ valley is closed (OFF). In the intrinsic p-type overall Ohmic contact of the germanene/GdI$_2$ and SiGe/GdI$_2$ vdWHs, as shown in Fig. 6e, both the K and K$'$ valleys participate in electron transport (ON), allowing free electron movement between the two valleys. As shown in Fig. 6b and g, by reversing the magnetization direction of Gd from $+z$ to $-z$, valley polarization is flipped, enabling the switching of the electron transport valley state between the K and K$'$ points. When combined with spintronics, magnetization reversal has the potential to create devices that couple spin and valley states, further expanding the range of possible applications. Adjusting the interlayer distance or electron/hole doping can regulate the contact type of the X/GdI$_2$ vdWHs to switch the electron transport channels in the K and K$'$ valleys, as shown in Fig. 6c, d and f, h, making them ideal candidates for valley-state logic devices. Fig. 6i and j schematically illustrates a valley-state logic device controlled by two gates (G_1 and G_2), with Dirac semimetals serving as the source and drain, connected by the 2D GdI$_2$ channel. The positive and negative voltages applied to G_1 and G_2 selectively regulate electron transport between the K and K$'$ valleys, enabling binary logic state encoding of "1" and "0" based on valley polarization. When the electric fields applied by both gates are in the same direction, both regions conduct through the same spin at either the K or K valley, and the device is in the on state ("1"). When the electric fields are opposite, the two regions conduct through opposite spins at the K and K$'$ valleys, and the device is in the off state ("0"). The ability to switch between half-valley and overall Ohmic contacts also facilitates the design of highly sensitive photodetectors that can selectively detect light with different wavelengths or polarizations, thereby enabling efficient photoelectric conversion. In the p-type overall Schottky contact of the X/GdI$_2$ vdWHs, as shown in Fig. 6c and h, due to the presence of the Schottky barriers, the electron transport channels in both the K and K$'$ valleys are closed (OFF). However, the nonlinear current–voltage characteristics of the p-type overall Schottky contact make the X/GdI$_2$ vdWH well-suited for rectifiers and Schottky diodes.

4. Conclusions

In summary, through first-principles calculations, we designed a class of p-type Ohmic contact vdWHs consisting of the valley-polarized semiconductor GdI$_2$ and Dirac semimetals X (X = graphene, germanene, and SiGe). Our binding energy analysis identified the T1-type stacking configuration as the most stable structure among different atomic alignments. Due to strong interlayer interactions and SOC effects, the Dirac semimetals exhibit band splitting and significant bandgap opening at their Dirac points. Meanwhile, the work function differences between GdI$_2$ and Dirac semimetals drive charge transfer from GdI$_2$ to the Dirac layers, inducing upward band bending in GdI$_2$ and shifting the Fermi level of the Dirac semimetals. Projected band structure analysis reveals that graphene/GdI$_2$ vdWH exhibits an intrinsic p-type half-valley Ohmic contact, while germanene/GdI$_2$ and SiGe/GdI$_2$ vdWHs form intrinsic p-type overall Ohmic contacts. Additionally, we demonstrate that interfacial charge transfer and SBHs in X/GdI$_2$ vdWHs can be precisely modulated through vertical strain engineering and electrostatic doping, enabling controlled transitions among half-valley Ohmic, overall Ohmic, and Schottky contact states. Notably, valley-switching ON/OFF behavior at the K and K$'$ points can be effectively regulated, offering a pathway for tunable valleytronic functionalities. This study provides valuable insights into valleytronic interface engineering and the design of valley-polarized semiconductors, paving the way for the development of highly efficient multi-state computing and storage devices with optimized carrier injection and ultra-low power consumption.

Author contributions

Hao Guo: conceptualization (equal); data curation (lead); formal analysis (lead); investigation (lead); validation (lead); visualization (lead); and writing – original draft (lead). Yongqian Zhu: conceptualization (equal); validation (supporting); visualization (supporting); and writing – review and editing (supporting). Jinbo Pan: supervision (lead); resources (supporting); and writing – review and editing (lead). Shixuan Du: resources (lead); supervision (supporting); and writing – review and editing (supporting).

Conflicts of interest

There are no conflicts to declare.

Data availability

The data supporting this article have been included as part of the ESI.†

Acknowledgements

This work was supported by the National Natural Science Foundation of China (No. 12202134), the National Key R&D Program of China (No. 2024YFA1207803 and No. 2022YFA1204100), the

Natural Science Foundation of Hebei Province (No. A2024407001), the Science Research Project of Hebei Education Department (No. BJK2024032), and the China Postdoctoral Science Foundation (No. 2024M763510). Computational resources were provided by the National Supercomputing Center in Tianjin.

References

1 L. Guo, S. Hu and X. Gu, *et al.*, *Adv. Mater.*, 2024, **36**, e2301854.
2 Y. Guo, X. Zhang and Z. Huang, *et al.*, *npj Spintronics*, 2024, **2**, 36.
3 D. Rani, P. C. Sreeparvathy and K. G. Suresh, *et al.*, *Phys. Rev. B*, 2023, **107**, 134434.
4 X. Zhao and F. Ma, *Phys. Lett. A*, 2020, **384**, 126494.
5 J. R. Schaibley, H. Yu and G. Clark, *et al.*, *Nat. Rev. Mater.*, 2016, **1**, 1–15.
6 Y. Tan, J. Zheng and X. Niu, *et al.*, *Sci. China: Phys., Mech. Astron.*, 2023, **66**, 117505.
7 C. Luo, Z. Huang and H. Qiao, *et al.*, *J. Phys.: Mater.*, 2024, **7**, 022006.
8 Y. Jiang, X. Zhang and H. Bai, *et al.*, *Appl. Phys. Lett.*, 2025, **126**, 053102.
9 W. Xun, C. Wu and H. Sun, *et al.*, *Nano Lett.*, 2024, **24**, 3541–3547.
10 L. Bawden, S. P. Cooil and F. Mazzola, *et al.*, *Nat. Commun.*, 2016, **7**, 11711.
11 J. Guo, Z. Lu and K. Wang, *et al.*, *J. Phys.: Condens. Matter*, 2021, **34**, 075701.
12 H. Huan, Y. Xue and B. Zhao, *et al.*, *Phys. Rev. B*, 2021, **104**, 165427.
13 K. Sheng, B. Zhang and H.-K. Yuan, *et al.*, *Phys. Rev. B*, 2022, **105**, 195312.
14 P. Zhao, Y. Dai and H. Wang, *et al.*, *ChemPhysMater*, 2022, **1**, 56–61.
15 M. Lan, Y. Li and S. Qiao, *et al.*, *J. Phys. D: Appl. Phys.*, 2023, **56**, 385103.
16 S. Li, Y. Hou and M. Zhou, *et al.*, *J. Appl. Phys.*, 2023, **134**, 213901.
17 W. Liu, J. Tong and L. Deng, *et al.*, *Mater. Today Phys.*, 2021, **21**, 100514.
18 H.-X. Cheng, J. Zhou and W. Ji, *et al.*, *Phys. Rev. B*, 2021, **103**, 125121.
19 K. Sheng, H. K. Yuan and Z. Y. Wang, *Phys. Chem. Chem. Phys.*, 2022, **24**, 3865–3874.
20 Z. Lin, Y. Liu and Z. Wang, *et al.*, *Phys. Rev. Lett.*, 2022, **129**, 027401.
21 B. Wang, X. Zhang and Y. Zhang, *et al.*, *Mater. Horiz.*, 2020, **7**, 1623–1630.
22 A. Kasten, P. H. Müller and M. Schienle, *Solid State Commun.*, 1984, **51**, 919–921.
23 R. Zacharia, H. Ulbricht and T. Hertel, *Phys. Rev. B: Condens. Matter Mater. Phys.*, 2004, **69**, 155406.
24 S.-D. Guo, Y.-L. Tao and G. Wang, *et al.*, *Front. Phys.*, 2023, **19**, 23302.
25 K. Zhang, X. Wang and W. Mi, *Phys. E*, 2024, **155**, 115836.
26 K. Sheng, Q. Chen and H.-K. Yuan, *et al.*, *Phys. Rev. B*, 2022, **105**, 075304.
27 S. Li, Y. Hou and M. Zhou, *et al.*, *J. Appl. Phys.*, 2023, **134**, 123901.
28 X. Zhou, R.-W. Zhang and Z. Zhang, *et al.*, *npj Comput. Mater.*, 2021, **7**, 160.
29 C. Wang and Y. An, *Appl. Surf. Sci.*, 2021, **538**, 148098.
30 F. Is, R. Ahammed and P. Nandi, *et al.*, *Appl. Surf. Sci.*, 2023, **611**, 155675.
31 X. Wang and J.-Y. You, *Mater. Today Electron.*, 2023, **5**, 100051.
32 J. X. Li, W. Q. Li and S. H. Hung, *et al.*, *Nat. Nanotechnol.*, 2022, **17**, 721–728.
33 Y. Wang, J. C. Kim and R. J. Wu, *et al.*, *Nature*, 2019, **568**, 70–74.
34 A. Allain, J. Kang and K. Banerjee, *et al.*, *Nat. Mater.*, 2015, **14**, 1195–1205.
35 X. Zhang, Y. Zhang and H. Yu, *et al.*, *Adv. Mater.*, 2023, **35**, e2207966.
36 Y. Liu, N. O. Weiss and X. Duan, *et al.*, *Nat. Rev. Mater.*, 2016, **1**, 16042.
37 D. S. Schulman, A. J. Arnold and S. Das, *Chem. Soc. Rev.*, 2018, **47**, 3037–3058.
38 F. Is, R. Ahammed and A. De Sarkar, *Nanoscale*, 2025, **17**, 10142–10154.
39 X. Feng, C. S. Lau and S. J. Liang, *et al.*, *Adv. Funct. Mater.*, 2023, **34**, 2309848.
40 G. Kresse and J. Furthmüller, *Phys. Rev. B: Condens. Matter Mater. Phys.*, 1996, **54**, 11169.
41 G. Kresse and J. Hafner, *Phys. Rev. B: Condens. Matter Mater. Phys.*, 1993, **47**, 558.
42 P. E. Blöchl, *Phys. Rev. B: Condens. Matter Mater. Phys.*, 1994, **50**, 17953–17979.
43 J. P. Perdew, K. Burke and M. Ernzerhof, *Phys. Rev. Lett.*, 1996, **77**, 3865–3868.
44 S. L. Dudarev, G. A. Botton and S. Y. Savrasov, *et al.*, *Phys. Rev. B: Condens. Matter Mater. Phys.*, 1998, **57**, 1505.
45 S. Grimme, J. Antony and S. Ehrlich, *et al.*, *J. Chem. Phys.*, 2010, **132**, 154104.
46 S. Grimme, S. Ehrlich and L. Goerigk, *J. Comput. Chem.*, 2011, **32**, 1456–1465.
47 J. Deisenhofer, H. A. Krug von Nidda and A. Loidl, *et al.*, *Phys. Rev. B: Condens. Matter Mater. Phys.*, 2004, **69**, 104407.
48 A. B. T. Ohta, T. Seyller, K. Horn and E. Rotenberg, *Science*, 2006, **313**, 951–954.
49 H. Zhou, M. Zhao and X. Zhang, *et al.*, *J. Phys.: Condens. Matter*, 2013, **25**, 395501.
50 P. Jamdagni, A. Kumar and A. Thakur, *et al.*, *Mater. Res. Express*, 2015, **2**, 016301.
51 T. P. Kaloni and U. Schwingenschlögl, *Chem. Phys. Lett.*, 2013, **583**, 137–140.
52 H. Chen, J. Zhao and J. Huang, *et al.*, *Phys. Chem. Chem. Phys.*, 2019, **21**, 7447–7453.
53 R. Chen, Y. Wang and G. Qian, *et al.*, *ACS Appl. Nano Mater.*, 2023, **6**, 3453–3462.
54 B. J. Cid, J. E. Santana and L. G. Arellano, *et al.*, *Appl. Surf. Sci.*, 2023, **610**, 155541.
55 Y. Ma, Y. Wu and J. Tong, *et al.*, *Nanoscale*, 2023, **15**, 8278–8288.

56 X.-j Dong and C.-W. Zhang, *Chin. Phys. B*, 2024, **33**, 077303.
57 Q. Cui, J. Liang and B. Yang, *et al.*, *Phys. Rev. B*, 2020, **101**, 214439.
58 X. Wei, M. Zhang and X. Zhang, *et al.*, *J. Phys. Chem. Lett.*, 2024, **15**, 3871–3883.
59 H. Wong, J. Zhang and J. Liu, *Nanomaterials*, 2024, **14**, 386.
60 L. Cao, X. Deng and Z. Tang, *et al.*, *Appl. Phys. Lett.*, 2022, **121**, 113104.
61 J. Li, W. Liu and W. Zhou, *et al.*, *Phys. Rev. Appl.*, 2022, **17**, 054009.
62 Y. Xue, L. Gao and H. Liu, *et al.*, *Appl. Surf. Sci.*, 2021, **555**, 149654.
63 Y. Liu, W. Zhang and B. Lv, *et al.*, *Surf. Interfaces*, 2022, **30**, 101823.
64 D. B. Zhang, Y. Hu and H. X. Zhong, *et al.*, *Nanoscale*, 2019, **11**, 13800–13806.
65 X. Liu, A. Islam and J. Guo, *et al.*, *ACS Nano*, 2020, **14**, 1457–1467.
66 K. Chen, X. Yan and J. Deng, *et al.*, *Nanoscale*, 2024, **16**, 3693–3700.
67 M. K. Mohanta, A. Arora and A. De Sarkar, *Phys. Rev. B*, 2021, **104**, 165421.
68 R. Meng, L. da Costa Pereira and J.-P. Locquet, *et al.*, *npj Comput. Mater.*, 2022, **8**, 230.
69 J. Xiao, Y. Wang and H. Wang, *et al.*, *Nat. Phys.*, 2020, **16**, 1028–1034.
70 A. M. Seiler, M. Statz and I. Weimer, *et al.*, *Phys. Rev. Lett.*, 2024, **133**, 066301.